A Switched Array Sounder for Dynamic Millimeter-Wave Channel Characterization: Design, Implementation and Measurements

Cai, Xuesong; Bengtsson, Erik L; Edfors, Ove; Tufvesson, Fredrik

Published in:
IEEE Transactions on Antennas and Propagation

2024

Document Version:
Peer reviewed version (aka post-print)

A Switched Array Sounder for Dynamic Millimeter-Wave Channel Characterization: Design, Implementation and Measurements

Xuesong Cai, *Senior Member, IEEE*, Erik L. Bengtsson,
Ove Edfors, *Senior Member, IEEE*, and Fredrik Tufvesson, *Fellow, IEEE*

***Abstract*—A prerequisite for the design and evaluation of wireless systems is the understanding of propagation channels. While abundant propagation knowledge exists for bands below 6 GHz, the same is not true for millimeter-wave frequencies. In this paper, we present the design, implementation and measurement-based verification of a re-configurable 27.5-29.5 GHz channel sounder. Based on the switched array principle, our design is capable of characterizing 128×256 dynamic double-directional dual-polarized channels with snapshot times of around 600 ms. This is in sharp contrast to measurement times on the order of tens-of-minutes of sounders by rotating horn antennas. The antenna arrays at both link ends are calibrated in an anechoic chamber with high angular sampling intervals of 3° in azimuth and elevation domains, which enables de-embedding the system responses of the sounder from the propagation channels. This is complemented with a bandwidth of up to 2 GHz, i.e., nanosecond-level delay resolution. The short measurement times and stable radio frequency design facilitate real-time processing of the received wavefronts to enhance measurement dynamic range. After disclosing the sounder design and implementation, we demonstrate its capabilities by presenting a measurement campaign at 28 GHz in an indoor lab environment.**

***Index Terms*—Channel sounder design, dynamic channels, mmWave, propagation measurements, switched arrays, parameter estimation.**

I. Introduction

The explosive growth of mobile data rates and the number of connected devices is motivating the use of spectrum previously unused for cellular communications [3–5]. As a result, frequency bands close to the millimeter-wave (mmWave) regime from 24.5-29.5 GHz have received considerable attention [4–6].[1] Spectrum in the 24-28 GHz band has been auctioned in the United States by the Federal Communications Commission, triggering rapid research and developments activities [7]. Other countries in North America, Europe, Asia and Oceania are following the same path. The Third Generation Partnership Project (3GPP) has also integrated mmWave frequencies into Release 15 and onward standardization of fifth-generation (5G) systems [8, 9]. Nevertheless, mmWave suffers from high omnidirectional free-space attenuation. Massive multiple-input multiple-output (MIMO) has thus been identified as an important technology in 5G and beyond, where beamforming is exploited to compensate severe power loss associated with the smaller antenna aperture for a satisfactory link signal-to-noise ratio (SNR) [10]. Meanwhile, beam management, including accurate and fast beam tracking, beam failure recovery, etc., is essential for communications with mobility [11]. Different polarizations are also utilized [10]. Therefore, for efficient design, performance assessment and deployment planning of mmWave systems, an in-depth understanding of how the mmWave channels behave and evolve in parameter domains of power, delay, Doppler frequency, double directions, dual polarizations, etc. is crucial. Examples efforts include IEEE standardization projects P1944 [12] and P2982 [13] for mmWave channel measurements and channel modeling. Given a common environment, mmWave channels behave differently from frequencies below 6 GHz [6]. Real-time mmWave channel measurement campaigns are indispensable for establishing realistic wideband *dynamic double-directional dual-polarized* models that capture the physics of the involved propagation processes.

To achieve this, a *channel sounder* needs to be designed. The fundamental principle of a channel sounder is to inject a known waveform into the channel, so that suitable signal processing is able to de-convolve the transmitted waveform out of the received signal, in turn acquiring the propagation channels. Steady progress is seen in the literature on channel sounder design at mmWave frequencies. Nevertheless, majority of the existing directional sounding setups are for indoor environments and are based on vector network analyzers (VNAs), which use slow chirp and/or frequency scanning,

X. Cai, O. Edfors, and F. Tufvesson are with the Department of Electrical and Information Technology, Lund University, Lund, Sweden (e-mail: {xuesong.cai, ove.edfors, fredrik.tufvesson}@eit.lth.se). E. L. Bengtsson is with Sony Research Center, Sony Europe, Lund, Sweden (e-mail: erik.bengtsson@sony.com). At the time of conducting this work, E. L. Bengtsson was also with the Department of Electrical and Information Technology, Lund University, Lund, Sweden. A small part of this paper was presented at the IEEE International Symposium on Antennas and Propagation (APS) 2020, Montreal, Canada [1]. Aspects of the sounder design were also discussed in [2], a Ph.D. thesis at Lund University, Sweden.

The authors acknowledge the contributions from Harsh Tataria and Carl Gustafson. The authors are thankful for valuable discussions with National Instruments Inc., Sony Semiconductor Solutions, and Ericsson AB during the design of the presented channel sounding system and fruitful discussions with Prof. Andreas F. Molisch at the University of Southern California, USA. The authors also acknowledge the help provided by Martin Nilsson, Meifang Zhu, and Juan Sanchez during measurement campaigns.

This work was supported in part by the Horizon Europe Framework Programme under the Marie Skłodowska-Curie grant agreement No. 101059091, the Swedish Research Council (Grant No. 2022-04691), the Royal Physiographic Society of Lund, the Strategic Research Area Excellence Center at Linköping–Lund in Information Technology (ELLIIT), and Ericsson.

[1] Following the conventional terminology in the related literature, we denote the frequencies 24.5-29.5 GHz as mmWave frequencies, even though, strictly speaking, they are below the "true" mmWave band which spans 30-300 GHz (see e.g., [6] and references therein).

combined with virtual arrays (mechanical movement of a single element or a set of antennas along a track). Such sounders struggle to capture *dynamic environments* and require a cabled connection between the transmitter and receiver limiting their separation distance [14–19], although optical fiber can help extend the cable length [20, 21]. For outdoor scenarios, the prevalent method for directionally resolved measurements is based on mechanically rotating horn antennas and measuring the channel impulse response for a fixed pair of transmit and receive orientations [4, 22–27]. There are two major limitations of such an approach: First is the *non-coherent* nature of the measurements, such that the obtained *angular resolution* is limited by the half-power beamwidth (HPBW) of the horn element. As a result, multipath components (MPCs) arriving from different directions may fall into the antenna beamwidth, yet appear as a *single* component. Thus, it has been difficult to predict the precise number of contributing MPCs in a given propagation environment and the fundamental question on mmWave channels being *sparse* (in the sense of having small number of MPCs) remains unanswered. Secondly, mechanical rotation of the horn element typically requires measurement run times on the order of tens-of-minutes or an hour to cycle through all antenna orientations along the azimuth and elevation domains (with a reasonable granularity, for a given snapshot at a particular location).

To overcome these limitations, several other systems have been reported in the mmWave propagation literature. For instance, the authors in [26] present a continuous-wave-based narrowband sounder operating at 28 GHz, feeding 22 dBm of transmit power into a 10 dBi horn antenna. The receiver comprises of a 24 dBi horn antenna mounted on a rotating platform which allows for a full 360° scan across the azimuth plane in 200 ms with 1° angular sampling. While this considerably reduces the measurement time, the single element at the transmitter limits the ability to measure truly dynamic, directional channels. Alternatively, the system presented in [28, 29] is one of the earliest to consider the possibility of measuring dynamic mmWave multiple-input multiple-output (MIMO) channels. The designed system can facilitate measurements across multiple frequency bands with a variable bandwidth of 3.5 GHz or more, and utilizes dual-polarized horn antennas at both transmit and receive link ends. Examples of the power azimuth and elevation spectra at 60 GHz are presented in [28]. Nevertheless, having dual-polarized horn antennas hugely constrains the total field-of-view of the transmitter and receiver. The authors in [30, 31] have proposed a sounder based on an *array* of directional horn antennas combined with fast switching at the receiver with a single transmit antenna. On the other hand, studies in [32, 33] present a multi-band MIMO channel sounder operating at 30 GHz, 60 GHz and 90 GHz with 8×8 and 2×2 antenna arrays, respectively. The MIMO operation is realized by employing switches at the intermediate frequency (IF) along with parallel frequency conversions. Nonetheless, the output transmit powers are limited to 16 dBm at 30 GHz, 7 dBm at 60 GHz and 4 dBm at 90 GHz, greatly reducing the dynamic range of the sounder. The authors in [34] present a sounder with 4 transmit antennas multiplexed with a single pole four throw (SP4T) switch and 4 receive antennas with 4 parallel down-conversion chains. Similar to [32], the transmit power is limited to 24 dBm. Collectively, the majority of the aforementioned works use the switched array principle. However, the MIMO order, i.e., the angle resolution, is limited, not being able to fully complement the delay resolution on offer. Furthermore, for dynamic environments, the vast majority of the reported measurements *either* investigate the angular characteristics without considering the temporal behavior of parameters, or focus on the temporal behavior without considering the angular characteristics - see e.g., [35, 36]. To the best of our knowledge, the sounder presented in [37] is the most complete thus far in terms of characterizing the amplitude, delay, angular and Doppler properties of the mmWave channel in dynamic outdoor scenarios. The system is based on the concept of a phased array and performs fast beam switching/steering (on the order of 2 µs) in both the azimuth and elevation domains with 8×2 arrays at the transmitter and receiver. However, this setup is restricted to measure over 90° sectors in azimuth and elevation, limiting the overall sounding field-of-view and hence MPC determination. Furthermore, in order to maintain the phase coherency across multiple radio-frequency (RF) down/up-conversion chains, the operational bandwidth was constrained to 400 MHz, which directly limits the delay resolution. The angular resolution is also restricted by the size of the arrays used at both ends with the active radiation patterns in [37].

To summarize, the inability to simultaneously obtain high-resolution dynamic characteristics and polarimetric bidirectional characteristics of mmWave channels is a serious defect of the existing mmWave channel sounders. To fill the research gap, we have developed a novel mmWave channel sounder in this paper. The contributions of the paper can be summarized as follows:

- We present the design, implementation and verification of a re-configurable switched array channel sounder operating at 27.5-29.5 GHz, capable of measuring 128×256 dynamic double-directional dual-polarized channels in around 600 ms. The highly stable RF design enables efficient field-programmable-gate-array (FPGA) implementation to carry out complex real-time averaging of multiple received waveforms, increasing the measurement SNR. The significant array gain obtained in the post-processing further enhances the dynamic range. Relative to state-of-the-art systems, the design provides superior angular resolution and is complimented with a nanosecond delay resolution. As such, the design presents an opportunity to *jointly* estimate and track the MPC parameters. Moreover, an overall field-of-view of around 180° at the transmitter and 360° at the receiver is achieved, enabling the detection of MPCs from a wide angular range.
- The active antenna radiation patterns at the transmit and receive arrays with the cascaded switching networks and interconnects are calibrated with a dense angular sampling of 3° in both the azimuth and elevation domains, over a 3 GHz band from 27-30 GHz with 10 MHz frequency steps. The granularity in angular sampling is

superior by an order-of-magnitude relative to most other systems and is considered to be extremely difficult and time consuming. The successful calibration is essential to de-embed the antenna patterns from the propagation channels, e.g., utilizing high-resolution channel parameter estimation algorithms.

- We present a sample propagation channel measurement at 28 GHz with a 768 MHz effective bandwidth in an indoor laboratory scenario. We extract the channel parameters of MPCs observed along the measurement trajectory using a high-resolution algorithm. The evolution of the MPCs in different parameter domains shows good consistency to the geometry of the propagation scenario, which gives confidence to the measured results.

The rest of the paper is organized as follows. Sect. II elaborates on the channel sounder design and implementation. Sect. III discusses the post-processing aspects mainly for high-resolution parameter estimation from measurement data. An indoor measurement campaign and the corresponding data-processing results are presented in Sect. IV. Finally, conclusive remarks are included in Sect. V.

II. Channel Sounder Design and Implementation

The general principle is as follows: A known waveform is generated at baseband and up-converted to the carrier frequency of interest, followed by amplification and transmission. On the receive side, the waveform is down-converted, sampled and stored for processing. The channel impulse response is extracted from the received signal envelope relative to the known waveform that was transmitted. In order to capture the directional characteristics, channel impulse responses of antenna combinations from the transmitter to the receiver are measured.

A. Sounding Waveform Design

Sounding waveforms are usually designed in accordance with the sounder type. They range from standard pulse trains [38, 39], pseudo noise sequences [40, 41], chirp signals [42, 43], or multitone sequences [14, 44]. In our design, two options for generating the baseband sounding waveform are implemented. The first option is to exploit the *Zadoff-Chu (ZC)* sequence. ZC sequences have ideal correlation properties in both time and frequency domains, and are thus well suited for channel sounding. In contrast to other waveforms, they are also easily scalable across both time and frequency domains. To obtain the complex samples of the waveform, a ZC sequence of a certain length is generated, pulse-shaped using, e.g., a root-raised-cosine filter with a roll-off factor of α, and up-sampled with an oversampling rate of β. The effective (nonzero-power) bandwidth of the transmitted waveform is jointly determined by α, β and the transmission rate r of the complex samples as $\frac{r(1+\alpha)}{\beta}$ and thus is reconfigurable. Note that the oversampling rate β should be non less than $(1+\alpha)$ to avoid aliasing. Naturally, wider *signal bandwidths* lead to higher delay resolutions, while the *total duration* of the sounding waveform is designed keeping in mind the largest possible delay of effective/observable MPCs. For example, complex samples of a length-2047 ZC sequence with $\alpha = 0$ and $\beta = 1$ and transmitted with a complex rate of 768 MHz lead to an effective bandwidth of 768 MHz, and are suitable for channels where the propagation delays of all effective MPCs are less than 2.7 μs, i.e., $\frac{2047}{768}$ μs.

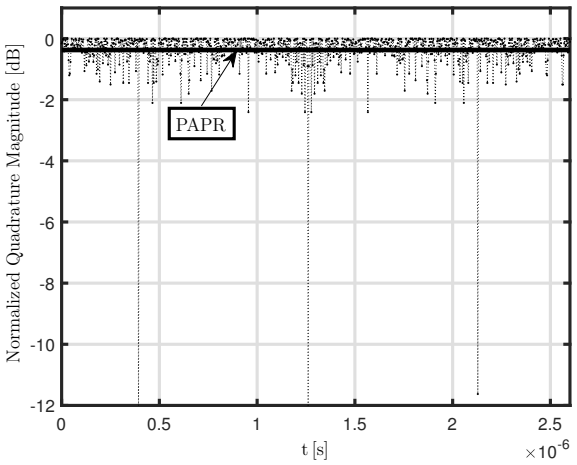

Fig. 1. Normalized quadrature magnitude of the multi-tone waveform in dB as a function of time with a PAPR of 0.349 dB.

In line with the setups in [30, 37, 44], a multi-tone baseband sounding waveform can also be implemented at the transmitter's host interface as a second option. Denoted by $x(t)$, the sounding waveform can be written as $x(t) = \sum_{n=-N}^{N} e^{j(2\pi n \Delta f t + \theta_n)}$. The total number of tones are given by $2N+1$, while Δf denotes the tone spacing, and θ_n is the complex phase of the n-th tone. Following the methodology presented in [37, 45], the values of θ_n are designed to optimize the peak-to-average-power ratio (PAPR) of $x(t)$ for power efficient signaling to maximize the forward link SNR. Fig. 1 depicts the normalized quadrature magnitude of $x(t)$ with 2000 tones, which is seen to have a PAPR within 0.35 dB. The low PAPR is beneficial to transmit with power as close as possible to the 1 dB compression point of the transmit power amplifier (PA). The effective bandwidth is similarly related to the oversampling rate of the time-domain complex samples and the transmission rate.

In addition, for greater robustness against measurement noise, *multiple* ZC waveforms or multi-tone waveforms are transmitted in real-time. At the receiver, the multiple received replicas are averaged and correlated with the transmitted waveform. We present further details of this in the subsection that follows. The above length-2047 ZC sequence with 768 MHz effective bandwidth is used for demonstrations throughout the paper.

B. Sounding Frame Structure

As it will be described in greater detail later in the paper, the sounder is designed with a 128 element uniform planar array (UPA) at the transmitter and a 256 element cylindrical array at the receiver supporting dual polarization. Both arrays are equipped with integrated RF switches to switch through each antenna combination from the transmitter to the receiver.

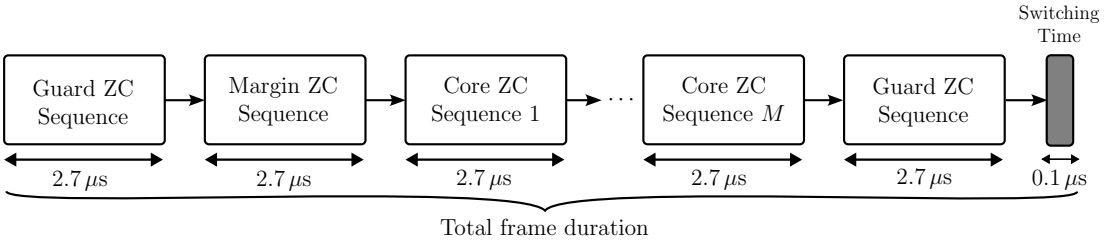

Fig. 2. Frame structure composing of two guard sequences, one margin sequence, M core sequences and switch settling time.

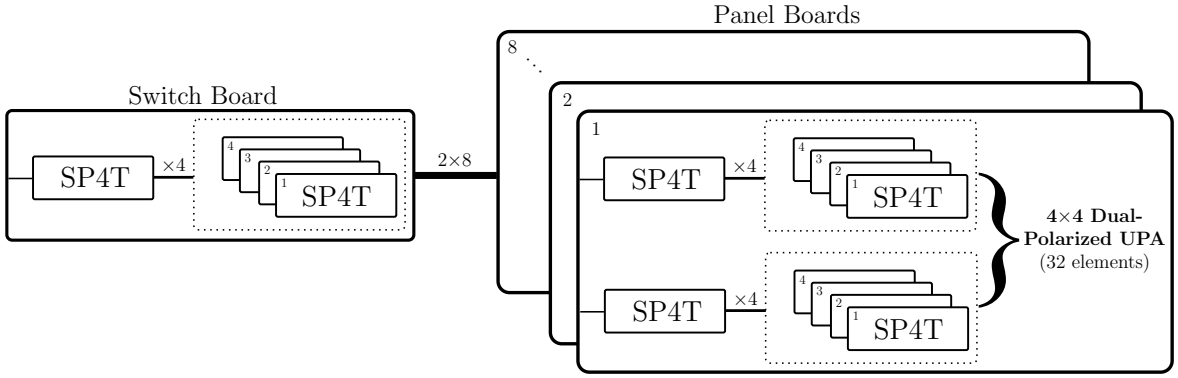

Fig. 3. The cascaded switching topology divided into a switch board feeding up to 8 antenna panel boards each with 16 dual-polarized antenna elements. This enables control of 256 elements. The same architecture is used for the 128 element array with 4 antenna panels instead of 8.

According to the switched array principle, both link ends are equipped with a single RF up/down-conversion chain. From each transmit antenna, the *frame structure* is built up from multiple repeated ZC sequences, followed by a *guard period* for settling the RF switches after activation. The guard duration of the RF switches is aligned with the 99% settling time of 100 ns for most commercial RF switches operating up to 44 GHz [46]. The number of ZC sequences transmitted from each antenna is re-configurable, and is a design parameter to strike the right balance between the total time taken to measure one antenna combination and robustness against measurement noise. In addition, the first and the last ZC sequence in each frame are added as *guard sequences* in case there are drifts from the clock source (CLK) which could cause the receiver to be out of synchronization from the transmitter (especially for calibrated CLKs used independently at both link ends). The second ZC sequence of the frame is used by the receiver as a margin because there are propagation delays and the received signal at the beginning of this frame can be from the previously activated transmit element. The remaining arbitrary number of core ZC sequences are used for real-time averaging. Since each ZC sequence is of duration 2.7 μs, the total frame duration with *four* ZC sequences for real-time averaging is given by 18.8 μs. To this end, with 128 transmit and 256 receive antennas, 32768 channel combinations yield a MIMO snapshot that can be measured in around 600 ms. Naturally, a lower number of core ZC sequences used for real-time acquisition reduces the duration of the MIMO snapshot. In the general case, the frame structure for any transmit-receive antenna combination with the number of core ZC acquisitions set to M is depicted in Fig. 2.

C. Transmit and Receive Architectures

We now present details on the designed antenna arrays and switching architecture, non-sequential switching, antenna array calibration, transmit and receive hardware, and real-time host as well as FPGA software implementation aspects. In order to maximize clarity, we distribute the aforementioned items into the different subsections below.

1) Antenna Arrays and Switching Architecture: In the literature, architectures based on switched arrays can be classified into *switched beam architectures* (SBA), *switched horn antenna arrays* (SHA), and *switched patch arrays* (SPA), respectively [4, 22–37, 47–50]. The major difference between these approaches relates to the achievable dynamic range and scalability of the design. The SBA achieves high gain by coherently combining signals from multiple elements, while the SHA achieves large array gains leveraging the horn antenna directivity. In contrast, the SPA digitizes the channel impulse response measured at each antenna to achieve array gain in the digital domain via further post-processing. For the SBA, a critical part of the circuit design is the phase-shifting network. Using standard complementary metal oxide semiconductor or gallium arsenide technology, an insertion loss on the order of 10 dB is expected with a moderate switching rate of 1 µs [51]. Thus, to fully exploit the array gain and overcome the insertion loss of the network, an amplifier (low-noise at the receiver or high power at the transmitter) between the element and the phase shifter is needed. This has a significant impact on power consumption, implementation complexity and cost when the number of elements are increased. Moreover, there is a fundamental practical limit to the beam switching rate, which should be fast enough for a small overall channel acquisition

time. The main limitation of SHA relates to cost, mechanical complexity and size, since each well designed horn element is expensive and needs to be arranged mechanically to cover a unique angle (see e.g., the array known as “Porcupine" used in [52], which is about 0.5 m in diameter). Different from SBA and SHA, the SPA design has the ability to utilize the recent advances in RF switching technology, significantly reducing the net insertion loss to less than 2 dB for a single switch with a switching rate on the order of 100 ns at mmWave frequencies [46]. This has opened up the prospects for massive SPA designs, such as the one presented as follows, offering the best trade-off solution in terms of implementation complexity, cost and performance.

Specifically, the antenna arrays employed at both the transmit and receive ends are composed of dual-polarized patch elements, and are interfaced with a quadruple-cascaded RF switching network. The switching circuitry needed to facilitate the design of the transmit/receive arrays is based on custom made 28 GHz SP4T switches donated by Sony Semiconductor Solutions. On average, the switches can sink 32 dBm and have a net insertion loss on the order of 1.5 dB - well exceeding the design specifications of commonly available commercial RF switches in the public domain. In general, the switching architecture enables control of up to 256 elements, and its design is divided into two parts: The first half is located on a dedicated *switch board* that carries two levels of cascaded switches and distributes the input signal to 16 coaxial connectors. The switch board is interfaced with the second half of the switching network, which is located at the backplane of individual *antenna element panels* (referred to as panel boards later in the text), where each panel has two coaxial inputs that are switched out to 32 antenna feeds compiled in a 4×4 UPA supporting two polarizations. For the 256 element receive array, there are eight such panels in an *octagon*, while for the 128 element transmit UPA, there are four panels in a *rectangle*. The overall cascaded switching topology supporting a maximum of 256 elements is shown in Fig. 3.

Both the switch board and antenna panel boards are designed with six-layer printed circuit board (PCB) technology based on Rogers RO4450B substrate with optimized loss tangent ($\tan(\tilde{\delta})$ = 0.004), dielectric constant (ϵ_r = 3.54±0.05), and above average thermal conductivity (0.6 - 0.8). The six layers of the PCB span 1020 μm of thickness in total. The process supports stacked vias through all six layers.[2] This enables a more compact layout with low insertion losses and has facilitated half of the switching circuitry to be at the back of the panels next to the feed of the patch elements. The front and backplanes of a single 32 element UPA panel are depicted in the left-hand side of Fig. 4. Note that the corrugation structure (horizontal stripes marked with the letter “B") is visible on the front view of the antenna panel above and below the patch elements. This was introduced to prevent surface currents from distorting the antenna radiation patterns and to minimize general energy spillover. However, due to manufacturing processing limitations, the required grounding

[2]We note that stacked vias enable signal paths to go through arbitrary layers of a PCB without introducing sidewise offsets.

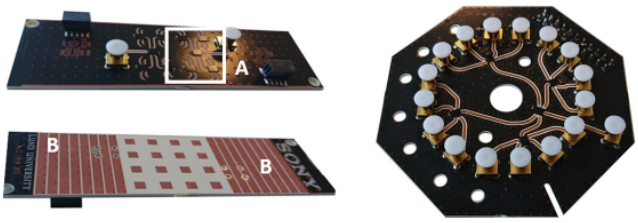

Fig. 4. Left-hand side: Fabricated 4×4 dual-polarized UPA panel with integrated switching. The rear part of the array containing the switching topology is demonstrated in the top half of the figure, while the bottom half contains the front of the array panel with the three-layered element design and corrugation structure for surface current minimization. Right-hand side: Switchboard with two layers of cascaded SP4T switches, coaxial connectors for input and 16 outputs with a control interface.

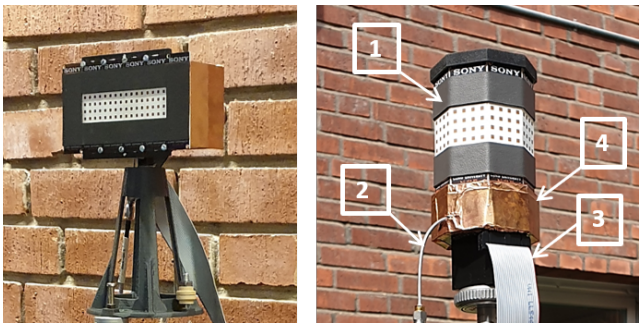

Fig. 5. Left-hand side: 128 element UPA for the transmitter; Right-hand side: 256 element octagonal array for the receiver. Both arrays contain the discussed integrated switches and control distribution networks.

associated with the corrugation structure could not be supported from a mechanical strength perspective. Instead, a layer of absorbing material (carbon induced rubber) was added, which will be visible later.

Each patch antenna seen on the left-hand side of Fig. 4 is designed as a *coupled parasitic resonator*, where the feed to the element is connected through stacked vias to the switch outputs (shown with a square with marker “A") at the panel backplane. The elements are designed in a three-layered structure: The lowest layer is the ground plane; the second layer elevated to 100 μm is a dual-feed coupling element; and the top layer at 300 μm, is the radiator. The coupling element in combination with the radiator generates two closely spaced resonances that are tuned to achieve a bandwidth that covers the desired measurement frequencies. We note that each element has been designed to deliver a HPBW in the azimuth of 85° and elevation of 50°. These are retained across both vertical and horizontal polarizations. In Sect. II-C3, we present details of antenna radiation pattern characterization and confirm the aforementioned HPBW values via measurements. For stable RF design, each element’s associated port is isolated by 20 dB with a -10 dB return loss over 26-30 GHz. The total insertion loss from the RF interconnects, cabling and switches is approximately 15 dB for each antenna. Each switchboard interface includes the first two layers of the switch cascade, and is equipped with a coaxial connector for feeding 16 coaxial connectors for signal distribution to the respective panels. This

is demonstrated on the right-hand side of Fig. 4. Using both the panel and switch boards, the transmit and receive arrays are shown in Fig. 5. As mentioned earlier, the corrugation structure on the panel boards of both arrays is overlaid with absorbing material (black) to minimize surface currents and leakage. On the receive array, this is marked by “1" on Fig. 5. The RF cable to/from the receive array is marked with “2". The 22-pol 8-bit transistor-transistor logic (TTL) control (cable) for antenna switching (maximum 256 states) is marked by “3", while the copper shielding for isolating the active control components suppressing unwanted radiation is shown with “4" on the receive array. The same trends can be observed for the transmit array with the exception of the shielding behind the array due to the location of the control blocks. Both arrays are further filled with absorbing material to avoid the creation of a cavity with resonances potentially leaking out.

2) Non-sequential Antenna Switching: As the aim of employing antenna arrays is to accurately extract the double-directional dual-polarized propagation parameters in dynamic scenarios, it is in general necessary to ensure that the MIMO cycle rate - the inverse of the duration between two adjacent snapshots should be greater than or equal to *two times* the maximum absolute Doppler shift, in order to avoid ambiguities in Doppler frequency estimation of MPCs. In a switched sounder, since the MIMO snapshot duration increases with the number of antenna combinations, there is an inherent conflict between the desired accuracy of the angle-of-arrival (AOA) and angle-of-departure (AOD) estimates (which implicitly demand higher numbers of antenna combinations) and the maximum admissible Doppler frequency. This limitation holds if the Doppler frequency is estimated relying on the Doppler-induced phase shifts among snapshots. In fact, when switched from one antenna combination to the other, the response variation already contains both Doppler-induced and antenna-induced (due to the change of antenna’s location and radiation pattern) effects. This implies that it is possible to rely on the responses of different antenna combinations for joint estimation of AOA, AoD and Doppler frequency. Nevertheless, if the array consists of regularly arranged antenna elements and they are sequentially switched, both the Doppler frequency and antenna switching could lead to linear phase shifts, meaning that there could be multiple solutions of angles and Doppler frequency that result in the same received signals, i.e., ambiguity in the joint estimation of angles and Doppler frequency [53, 54]. The authors of [53] were the first to report that the choice of *sequential* antenna switching sequence was causing this ambiguity. In a similar line, authors of [55, 56] introduced the normalized sidelobe levels as the objective function to derive the necessary conditions of array switching sequence which leads to ambiguities. Instead, by applying *randomized* (non-sequential) antenna switching, the antenna-induced phase shifts can be non-linearized, thus having the potential to greatly nullify the aforementioned ambiguities and extend the Doppler frequency estimation range to be close to half the inverse of the duration between two adjacent antenna-combination measurements. Hence, similar to [53, 57], we employ optimized *pseudo-random* switching at both link ends of our sounder, where the switching sequence is obtained by minimizing the level of ambiguity using the simulated annealing algorithm [57]. From an implementation viewpoint, both sides of the sounder activate antenna elements according to a predefined codebook that is known to both ends.

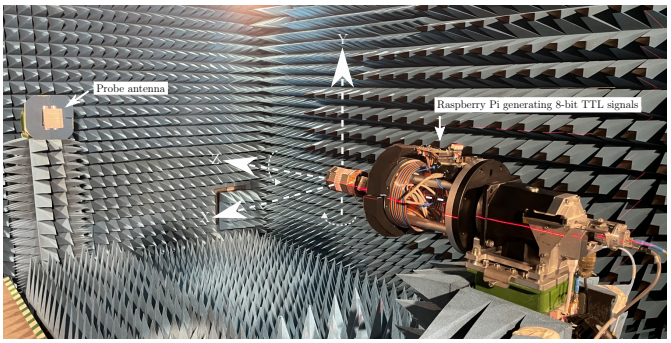

Fig. 6. Anechoic chamber measurement setup for characterization of the per-element gain and phase patterns of the fabricated antenna arrays from 27-30 GHz.

3) Antenna Array Calibration: The three-dimensional gain and phase patterns over both polarizations for both antenna arrays were characterized in an anechoic chamber of dimensions 9.5 m $\times$ 4.7 m $\times$ 3.8 m (length $\times$ width $\times$ height). The arrays were calibrated across 27-30 GHz (3 GHz bandwidth) with a frequency step size of 10 MHz. In order to maximize the sensitivity of the arrays when used with high-resolution post-processing, characterization of both arrays was done with a dense angular sampling of 3° in the azimuth and elevation. Fig. 6 illustrates the measurement setup with the 256 element array. A high-gain linearly-polarized antenna [58] was utilized as the probe antenna. By rotating the probe antenna, its polarization can be swapped in order to measure the patterns of two polarizations for each antenna element. The device under measurement (DUM), i.e., the antenna array, was mounted on a rotating arm which was controlled by a programmable positioner. The measurements utilized the classical *roll-over azimuth* principle to obtain the patterns over a sphere. Specifically, the center of the DUM was aligned to the origin of the coordinate system as shown in Fig. 6. The rotating arm rotated around the y-axis, i.e., rotated the coordinate system around the y-axis, to change the elevation of the probe, and rotated around the z-axis to change the azimuth of the probe. The distance from the probe to the origin of the coordinate system was 3 m, which is larger than the Fraunhofer distance of the array. The element switching for both DUMs was controlled by a computer (Raspberry Pi) interfacing with a switch control circuit leading towards the 8-bit TTL signals utilized by RF switches on the backplane of the antenna panels. To separate the antenna characteristics from the rest of the transmitter/receiver circuitry of the sounder, the DUMs were calibrated without the PA or low-noise amplifier (LNA). Together with the large number of elements, the dense sampling of the field in azimuth and elevation with the wide measurement bandwidth yielded an unusually high number of physical movements of DUMs.

After performing the measurements, the element gain and phase patterns in both polarizations across the measurement

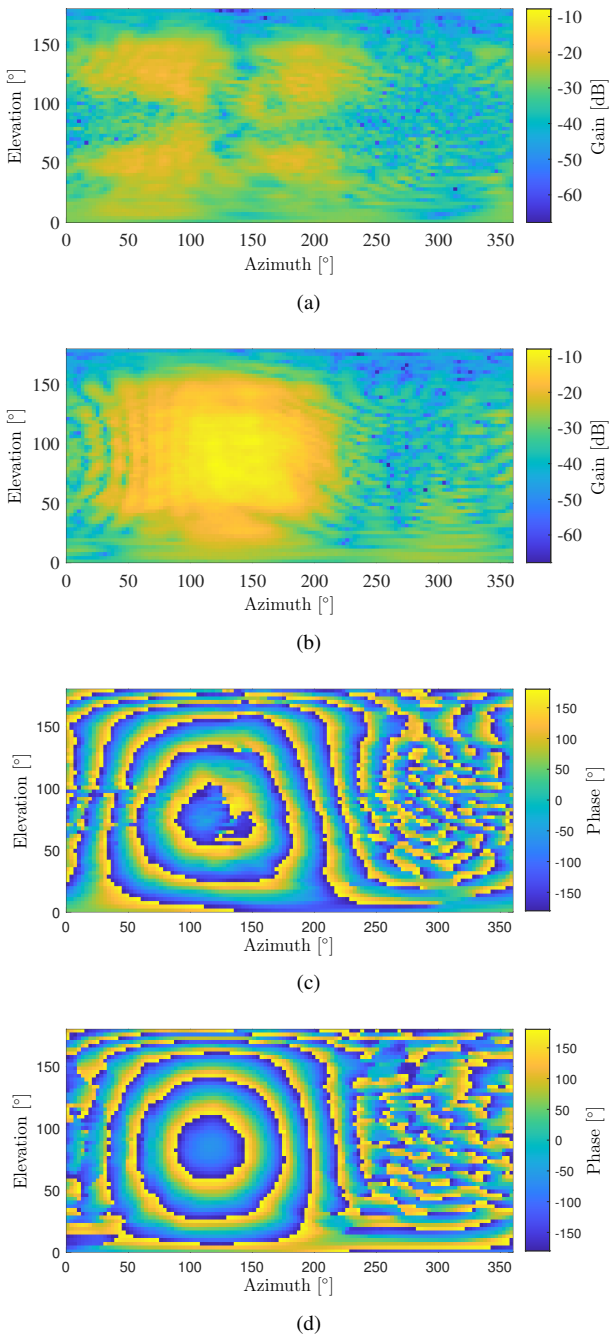

Fig. 7. Measured three-dimensional gain and phase radiation pattern of element 17 of the receive array at 28 GHz. This element is primarily vertically polarized. (a) Gain pattern of horizontal polarization with its maximum as -7.9 dB. (b) Gain pattern of vertical polarization with its maximum as -17.7 dB. (c) Phase pattern of horizontal polarization. (d) Phase pattern of vertical polarization.

bandwidth were analyzed. As indicated in Fig. 3, the receive array and transmit array both contain half vertically polarized elements and half horizontally polarized elements. Figs. 7 and 8 show example patterns at 28 GHz from antenna element 17 (primarily vertically polarized) at the receive array and from antenna element 45 (primarily horizontally polarized) at the transmit array, respectively. For both figures, one can extract several trends: Firstly, the radiation efficiency is maximum towards the broadside direction of the elements seen from the subfigures of gain patterns of both Figs. 7 and 8. Secondly, for the primary polarization mode, the earlier quoted azimuth and elevation HPBWs of 85° and 50° are confirmed. Thirdly, the cross-polarization discrimination ratio (i.e., the power present in the primary polarization relative to the non-primary polarization) is approximately more than 10 dB, and is retained across both array elements.

For the non-primary polarization mode, the element phase retains its overall shape but is as expected distorted relative to the phase of the primary polarization. This can be observed by examining the subfigures (c) and (d) in both figures, respectively. Although not shown here due to space constraints, the measured gain and phase patterns of the remaining elements of both arrays show equivalent trends as those described above. We now describe the transmit and receive hardware operation of the designed sounder.

4) Sounder Operation With Transmit and Receive Hardware: The transmitter is implemented and controlled in real-time with the National Instrument PXI-e 1085 chassis, supported by National Instrument's LabVIEW framework for software interfacing and control. The left-hand side of Fig. 9 shows the overall implementation of the transmitter hardware, where the physical circuit blocks are categorized and labeled from "A" to "G". Each of these corresponds to the right-hand side of the figure where the realized transmitter setup is depicted. As it can be observed from the design of the transmitter, parts of its operations are controlled by the local host PC (see "A" on the figure), while others require integration with an FPGA (denoted with "F"). The earlier explained frame structure (including the ZC sounding waveform with M = 4) is generated at the host, and is shaped with root-raised-cosine filtering before interfacing to the FPGA for repetitive transmission. The transmission process triggers the timing control governed by the FPGA, which receives an external 10 MHz CLK reference (shown as "G"). Similar to the designs in [30, 37], the CLK used for the sounding setup is based on a rubidium reference and is extremely stable with short-term stability less than 2×10^{-12} for 100 seconds [59]. A 14-bit digital-to-analog converter (DAC) output (shown as "B") is fed to an IF unit for mixing the baseband signal to an IF centered at 10 GHz via the aid of a frequency synthesizer. The IF output is then fed to the transmit RF head unit (marked with an "D") to be filtered and pre-amplified before up-conversion to the desired mmWave band at 28 GHz. As marked by * on the left-hand side of the figure, where applicable, the parameters quoted in the design are re-configurable to cover a 2 GHz bandwidth from 27.5 - 29.5 GHz when extending the parameters reported to cater for the bandwidth adjustment. This is also true when scaling down the bandwidth, to say

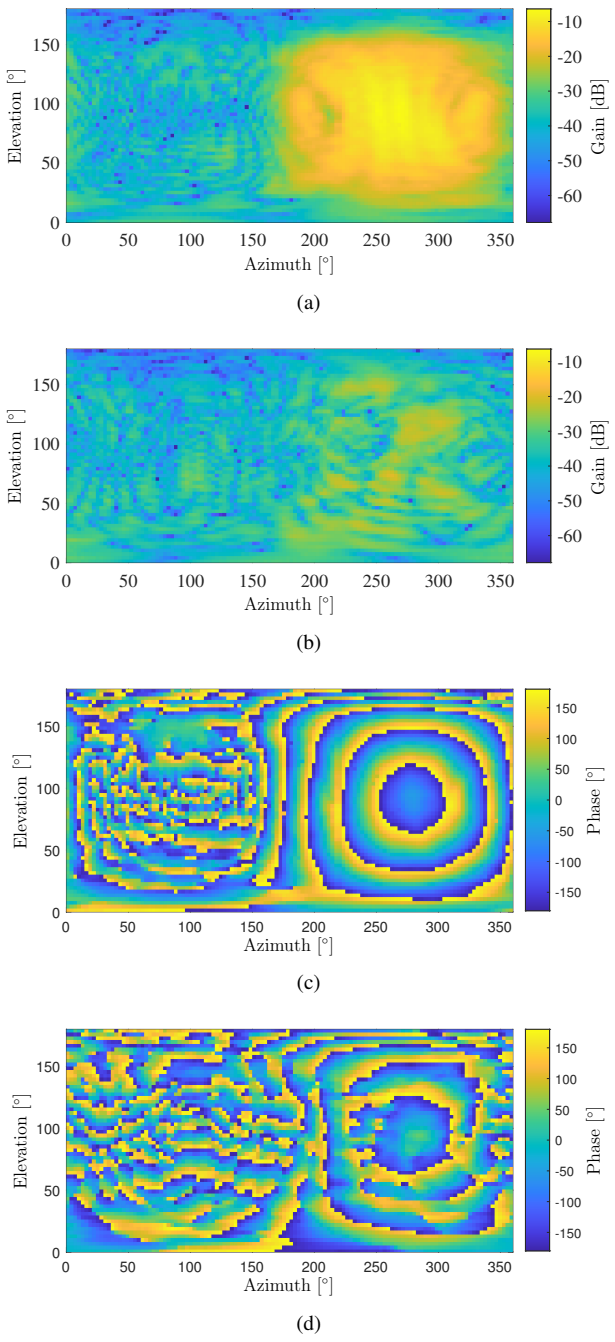

Fig. 8. Measured three-dimensional gain and phase radiation pattern of element 45 of the transmit array at 28 GHz. This element is primarily horizontally polarized. (a) Gain pattern of horizontal polarization with its maximum as -6.4 dB. (b) Gain pattern of vertical polarization with its maximum as -19.8 dB. (c) Phase pattern of horizontal polarization. (d) Phase pattern of vertical polarization.

TABLE I
TRANSMITTER AND RECEIVER SYSTEM COMPONENTS OF THE DESIGNED CHANNEL SOUNDER. UNLESS OTHERWISE STATED, THE LISTED COMPONENTS APPLY TO BOTH LINK ENDS.

Part Number	System Unit	Manufacturer and Model Number
1	PA	Sage Millimeter Inc., SBP-2633332228-KFKF-S1
2	LNA	Pasternack Inc., PE15A3300
3	Transmitter RF Head	NI 3642
4	Receiver RF Head	NI 3652
5	LO and IF Blocks	NI PXI-e 3620
6	DAC	NI PXI-e 3610
7	ADC	NI PXI-e 3630
8	FPGAs	NI PXI-e 7976 R, PXI-e 7902
9	Switch Control	NI 6581 B
10	Timing and Synch. Modules	NI PXI-e 6674 T
11	Host PC Framework	NI PXI-e 8880
12	Chassis Control	NI PXI-e 1085
13	Fast Array Hard Drive	NI PXI-e HDD 8261
14	CLK Source	Stanford Research Systems FS725

TABLE II
OVERALL SPECIFICATIONS OF THE DESIGNED CHANNEL SOUNDER. THE PARAMETERS WHICH CAN BE RE-CONFIGURED ARE LISTED WITH "(RE-CONFIGURABLE*)".

Parameter	Value
Sounder type	Switched array
Center frequency	28 GHz (re-configurable*)
Instantaneous bandwidth	Up to 2 GHz (re-configurable*)
Antenna array sizes/configurations	128 by 256/UPA and cylindrical (transmit and receive)
Azimuth/Elevation 3 dB beamwidths	85°/50°
Overall field-of-view at transmitter/receiver	180°/360°
Polarization	Dual (horizontal and vertical) (re-configurable*)
Receiver noise figure	5 dB
PA Gain and $P_{1\,\mathrm{dB}}$	22 dB, 28 dBm
LNA gain	43 dB
ADC/DAC resolution	12/14 bits
Switching rate	18.8 μs (re-configurable*)
MIMO snapshot rate	Around 600 ms (re-configurable*)
Switching sequence	Pseudo-random via a codebook (re-configurable*)
Transmitter-receiver CLK synchronization	Rubidium reference
Transmitted waveform duration	2.7 μs (re-configurable*)
ZC sequence length	2047 (re-configurable*)

500 MHz. A separate PA providing a maximum output power of 28 dBm is attached prior to the earlier described RF switching topology, while the CLK also triggers the switch timing (see "E" on the figure). A control signal activates one of the pseudo-random switch states according to the predefined codebook known to both transmitter and receiver, forwarding the mmWave signal to the desired antenna port for transmission over-the-air. Later we provide specific part details of the used circuit blocks.

The corresponding architecture at the receiver is shown on the left-hand side of Fig. 10. In accordance with the same predefined codebook as for the transmitter, the receive antenna elements and its associated switch circuitry is controlled via the CLK reference signal which triggers the capturing of the received waveform. This is followed by an LNA, and a down-converter to IF before being further mixed and low pass filtered (LPF) to baseband. A 12-bit analog-to-digital converter (ADC) is then employed to digitize the received analog waveform. The receiver FPGA is then used to perform

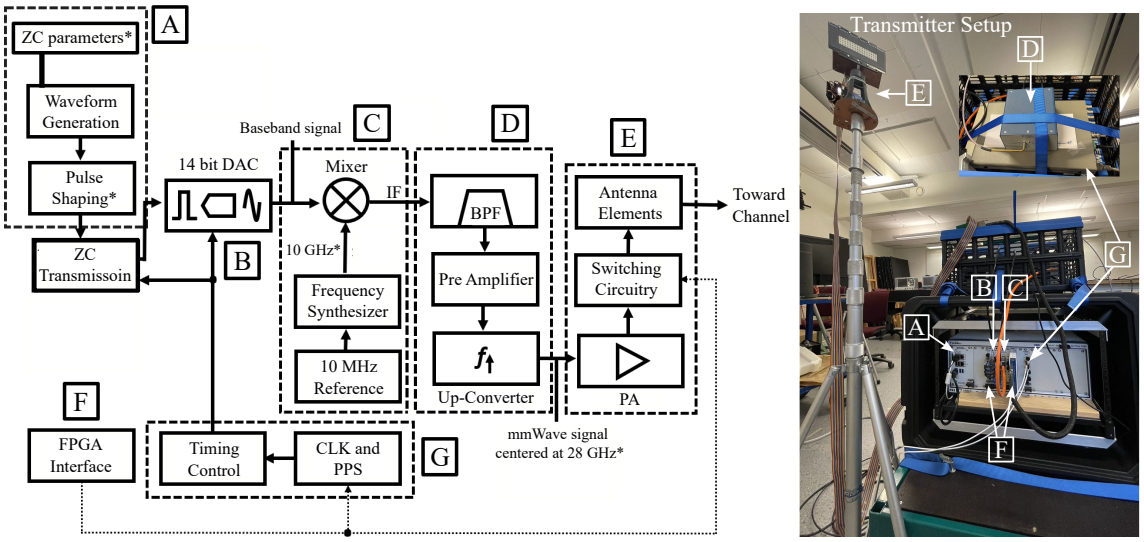

Fig. 9. Left-hand side: Overall design of the transmitter hardware architecture for switched array operation between 27.5-29.5 GHz. The annotations “A" to “G" denote the various transmitter circuit components, mapping to their physical make up as shown on the right-hand side of the figure. These are further described in the text. The terms “PPS" and “BPF" are read as “pulse per-second" and “bandpass filter", respectively.

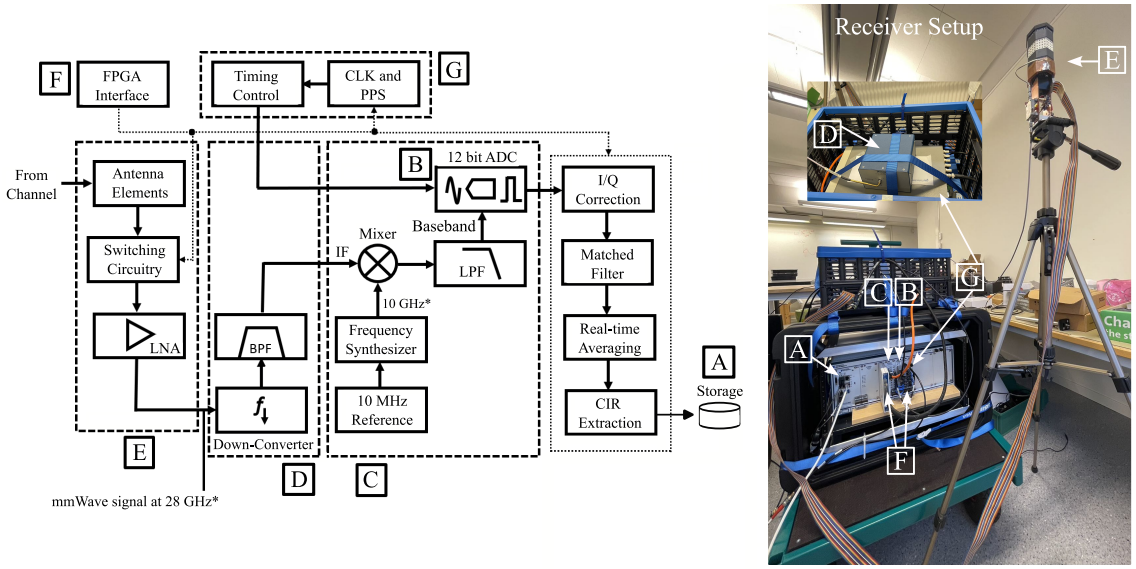

Fig. 10. Left-hand side: Overall receiver hardware for switched array operation between 27.5-29.5 GHz. The annotations “A" to “G" represent the various receiver circuit components, mapping to their physical equivalents as shown on the right-hand side of the figure. The terms “LPF", “I/Q", and “CIR" denote “low-pass filter", “in-phase/quadrature", and “channel impulse response”, respectively.

in-phase/quadrature (I/Q) sample correction to remove the DC offset and I/Q imbalance of the received signals, followed by a power maximization stage introduced by a matched filter (MF). The FPGA performs real-time averaging of the many acquired replicas of ZC sequences, and the resulting average is *correlated* with the original ZC sequence to extract the channel impulse responses that are sent for storage and further post-processing to extract the directional propagation parameters. *Due to the large number of elements being switched at both the transmitter and receiver (32768 combinations in a snapshot), we stress that the above process is very complex and requires optimization of both hardware as well as real-time software.*[3] The terms “A" to “G" on the left-hand side of the figure categorize the system components and are depicted physically on the right-hand side where the complete receiver setup is shown. The receiver hardware is also interfaced with a National Instrument PXI-e 1085 chassis, controlled by the custom designed host and FPGA LabVIEW software frameworks. For both the transmitter and receiver, the different utilized circuit parts are provided in Table I.

[3]The processing also involves calibration and addition of metadata, e.g., absolute timing and antenna pair identification, which are not mentioned for the sake of maintaining clarity.

5) Key Real-Time Software Implementation Aspects: From a real-time software viewpoint, both the transmit and receive sides have a similar overall code framework. The code is divided in *three* parts: (1) Host code; (2) FPGA signal processing code, and (3) FPGA switch control code. The host code is the main controller, and acts as a user interface at both sides. It mainly controls the operational states and executes: (1) The ZC waveform, (2) The number of ZC repetitions, and (3) The number of switch states, i.e., the codebook. At the receiver, it additionally receives the raw channel impulse responses and adds the required metadata (absolute times, antenna pair indices, etc.) before saving. Unlike the host implementation, the signal processing FPGA code is clocked by the rubidium reference. The ZC signals are transmitted with the pre-defined number of repetitions, and the switch guard times are added together with a switch triggering signal which is generated between each frame. The receive side, similarly, processes each frame, generates a switch triggering signal across the received frames and sends the resulting channel impulse response with a timing identifier added to the host. The aforementioned processing involves synchronization, averaging and correlation of the received ZC waveform to the original ZC signal. The switch FPGA code is the least complex of the three, and is reused at both link ends. Its main role is to change the switch states based on the pre-defined codebook (defining the pseudo-random switching combinations) each time it receives a trigger signal from the real-time signal processing FPGA code. With the major aspects of the sounder design concluded, we now present the final specifications of the sounder and assess the sounder's dynamic range in order to understand its maximum measurable range.

D. Final Sounder Specifications and Dynamic Range

The overall specifications of the sounder are given in Table II. As shown by the tabulated entries, our design offers an unprecedented degree of re-configurability which can be exercised in-between measurements without any changes to the hardware. In particular, the center carrier frequency, bandwidth, total number of measured channels, number of active polarization modes, the total number of ZC sequences, and the switching sequence configuration can be re-configured depending on the measurement campaign. This enables, for instance, to get faster switching rates in either azimuth/elevation for one polarization mode for high mobility situations. In contrast, for more static channels, a longer measurement can be made for getting a detailed description of the channel conditions. This provides a considerable advantage relative to existing setups summarized in Sect. I of this paper, which cannot be re-configured instantaneously without extensive mechanical modifications to the sounder structure and re-cabling.

Fig. 11 depicts a link budget analysis of the sounder to figure out the maximum measurable power loss caused by the wireless propagation. The criterion is that the power of a path in the received channel impulse response should be higher than the noise power floor. As shown in Fig. 11, the sounder is expected to work at its maximum power capacity, i.e., 25 dBm is output by the PA.An antenna element integrated into the

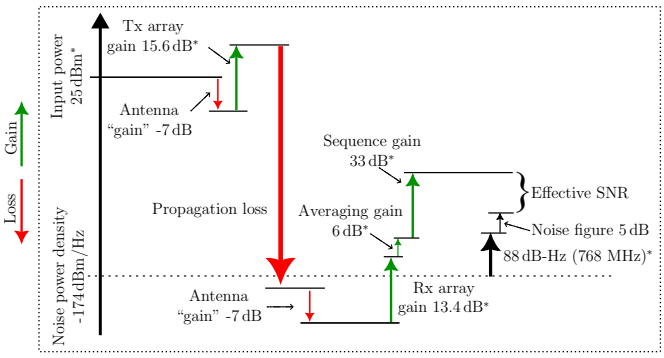

Fig. 11. An example link budget analysis for the sounder. The values which can be re-configured are marked with *. Although the input power is also adjustable, it is preferred that the sounder works at its maximum power capacity for the largest dynamic range.

switch panel radiates the signal out towards the channel, giving it a "gain" of around -7 dB. Then the signal is attenuated due to the propagation loss, followed by a "gain" of around -7 dB from a receive antenna element. Nevertheless, there are several processing gains to be included. By coherently combining the signals received at all antenna combinations, array gains can be harvested at both sides, which correspond to around 15.6 dB and 13.4 dB at the transmitter and receiver[4], respectively. The array gains are calculated by checking the measured responses of arrays in Sect. II-C3. Moreover, the sequence gain by exploiting the length-2047 ZC sequence is 33 dB. The averaging gain using 4 repeated ZC sequences corresponds to 6 dB. As for the noise power, we consider the noise power density -174 dBm/Hz at room temperature, with the effective bandwidth of 768 MHz, i.e., 88 dB-Hz. Moreover, cascading the individual noise figures of the circuit components shown in Fig. 10, the estimated noise figure for the receiver is around 5 dB. According to the above, the effective SNR of a path in the channel impulse response with processing gains can be calculated. By setting the threshold for the effective SNR as 0 dB, the maximum measurable propagation loss is attained as around 160 dB. Despite a large number of channels being measured within short times with both high spatial and temporal resolutions, this compares well with existing sounders reported in [31, 32, 37, 48]. Although the state-of-the-art rotating horn antenna sounder in [25] can measure power loss up to 185 dB, it is at the expense of much larger measurement durations since its design is based on a sliding correlator and is thus suitable only for static channel characterization. If the same measurement duration is applied, with our design, we could repeat the same static snapshot hundreds of times, which would further increase the maximum measurable power loss well beyond 185 dB.

III. Post-Processing Aspects

A. Channel Impulse Response and Channel Transfer Function

The channel impulse response of the measured propagation channel can be represented as a fourth order tensor denoted

[4]Not all antennas at the receiver can receive the same path effectively due to the cylinder array structure, causing a smaller array gain.

by $\mathbf{h}(\tau, s, m_{\mathrm{T}}, m_{\mathrm{R}})$. Here τ denotes the propagation delay, s denotes the measured snapshot index, m_{T} is the transmit antenna index, and m_{R} is the receive antenna index. The channel transfer function is then denoted by $\mathbf{H}(f, s, m_{\mathrm{T}}, m_{\mathrm{R}})$, where f denotes the frequency and is obtained via Fourier transform. The spatio-temporal information of the MIMO channel can be obtained from either $\mathbf{h}(\tau, s, m_{\mathrm{T}}, m_{\mathrm{R}})$ or $\mathbf{H}(f, s, m_{\mathrm{T}}, m_{\mathrm{R}})$.

B. MPC Parameter Estimation

Utilizing the dense spatial and temporal resolutions on offer with the designed sounder, our ultimate interest is to obtain propagation channel characteristics that are *independent* of the antenna architectures, such that the true directional properties of only the MPCs can be evaluated. Naturally, to do this, we would need to obtain a double-directional characterization of the channel that extracts the spatio-temporal polarimetric parameters of the MPCs from the transfer function via the use of a high-resolution estimation algorithm. Several approaches exist in the literature to do this, including expectation-maximization (EM) [60], space-alternating generalized expectation-maximization (SAGE) [61], CLEAN [62], RIMAX [63–65], and their variants such as [66, 67]. All of these approaches attempt to extract the directional MPC parameters in the maximum likelihood sense. These approaches are subjected to different model assumptions and underlying conceptual restrictions including applicability to certain antenna array architectures, calculation time in terms of convergence speed, and statistical efficiency.

The signal model of the measured channel transfer function is considered as a superposition of specular MPCs, and it is assumed that the geometrical propagation parameters of MPCs are unchanged during the observation time of S snapshots. The specular MPCs are characterized via plane waves through their delays (τ), Doppler frequencies (ν), azimuth and elevation AOAs (ϕ_{R} and φ_{R}), azimuth and elevation AODs (ϕ_{T} and φ_{T}), and complex polarimetric path gains (γ), such that $\boldsymbol{\Theta_\ell} = [\tau_\ell, \nu_\ell, \phi_{\mathrm{R},\ell}, \varphi_{\mathrm{R},\ell}, \phi_{\mathrm{T},\ell}, \varphi_{\mathrm{T},\ell}, \boldsymbol{\gamma}_\ell]$ is for the ℓ-th path. Analytically,

$$\begin{aligned}&\mathbf{H}(f, s, m_{\mathrm{T}}, m_{\mathrm{R}}; \boldsymbol{\Theta})\\ &= \sum_{\ell=1}^{L} \mathbf{b}_{m_{\mathrm{R}}}^{T}(\phi_{\mathrm{R},\ell}, \varphi_{\mathrm{R},\ell}, f) \begin{pmatrix} \gamma_{\mathrm{HH},\ell} & \gamma_{\mathrm{HV},\ell} \\ \gamma_{\mathrm{VH},\ell} & \gamma_{\mathrm{VV},\ell} \end{pmatrix} \mathbf{b}_{m_{\mathrm{T}}}(\phi_{\mathrm{T},\ell}, \varphi_{\mathrm{T},\ell}, f)\\ &\times \mathbf{b}(f)\, e^{-j2\pi f \tau_\ell} e^{j2\pi \nu_\ell t_{s,m_{\mathrm{T}},m_{\mathrm{R}}}} + \mathbf{N}(f, s, m_{\mathrm{T}}, m_{\mathrm{R}}),\end{aligned} \tag{1}$$

where $\boldsymbol{\Theta} = [\boldsymbol{\Theta_1}, \cdots, \boldsymbol{\Theta_L}]$ contains the path parameters of all L MPCs, $t_{s,m_{\mathrm{T}},m_{\mathrm{R}}}$ indicates the time instant when the channel between the m_{T}-th transmit antenna and the m_{R}-th receive antenna of snapshot s is measured, $(\cdot)^T$ denotes the matrix transpose operator, and N denotes white Gaussian noise. Moreover, $\mathbf{b}_{m_{\mathrm{R}}} \in \mathbb{C}^{2\times 1}$ and $\mathbf{b}_{m_{\mathrm{T}}} \in \mathbb{C}^{2\times 1}$ denote the mapping from the azimuth and elevation AOA and AOD to the corresponding polarimetric responses of the the m_{R}-th receive antenna and the m_{T}-th transmit antenna, respectively. Note that the mapping is also dependent on frequency f due to the frequency-dependent response of each antenna across the large bandwidth. The mapping is realized via the effective aperture distribution function (EADF) [68, 69] of both transmit and receive arrays based on the measurement data obtained in Sect. II-C3. The EADF is a known procedure that can facilitate gradient-based optimization/search in measurement-based parameter estimation. Essentially, at each frequency point, 2D discrete Fourier transforms are applied to the measured patterns to obtain spectra in the spatial-frequency domains that can be utilized afterward to recover antenna patterns via inverse transforms [68]. It also has the advantage of data compressing by keeping only the principal components in the spatial-frequency domain. The parameters $\gamma_{\mathrm{HH},\ell}$, $\gamma_{\mathrm{HV},\ell}$, $\gamma_{\mathrm{VH},\ell}$ and $\gamma_{\mathrm{VV},\ell}$ denote the horizontal-to-horizontal, horizontal-to-vertical, vertical-to-horizontal and vertical-to-vertical polarization gains of the ℓ-th MPC. Furthermore, $\mathbf{b}(f)$ represents the response of the system without antenna arrays, which can be obtained from the back-to-back measurement.

From (1) it is clear that parameters in $\boldsymbol{\Theta}$ associated with the L specular MPCs are to be estimated. Note that there is a major improvement compared to previous works. The frequency-dependent antenna responses across the wide bandwidth are observed, characterized and considered, leading to a much more realistic signal model, although this in turn breaks the Kronecker-product structure assumed in the conventional signal model [63], causing higher complexity in parameter estimation. By combining the advantages of EM and SAGE principles and improving the EADF-related likelihood optimization, we propose a new algorithm in the maximum-likelihood sense that can well overcome the complexity issue for high-resolution estimation of $\boldsymbol{\Theta}$. Since the detailed formulation of the algorithm is out of the scope of this paper, interested readers are referred to [70] for more information.

IV. Sample Measurement Results

A. Measurement Scenario

To validate the performance of the designed sounder, we present results from an indoor measurement campaign carried out in the E-Building, Department of Electrical and Information Technology (EIT), Lund University, Sweden. Fig. 12 depicts the scenario, i.e., a laboratory of $6.1\times5.5\times2.6$ m^3 with tables, shelves, equipment, etc. The transmitter location was fixed and is marked with a red dot (labeled as "Tx"), and the Rx was moving continuously along the green trajectory with a speed of around 0.1 m/s. One snapshot was recorded per second, and in total 29 snapshots were recorded along the trajectory. Note that the Rx stopped moving for the last 6 snapshots, resulting in the trajectory length being around 2.1 meters. The orientations of the arrays were always kept unchanged. As indicated in Fig. 12, the front panel of the Tx array was towards the wall "A", and the third panel of the Rx array was towards wall "B" for all snapshots along the trajectory. The measurement was conducted using all antennas at both link ends (i.e., measuring 32768 channel combinations) with a center frequency of 28 GHz and an effective bandwidth of 768 MHz. The parameters of MPCs for each snapshot were estimated using the principle outlined in Sect. III-B.

B. Measured Results and Evaluations

Fig. 13 illustrates two channel impulse responses obtained for the first snapshot and the twentieth snapshot, respectively,

(a)

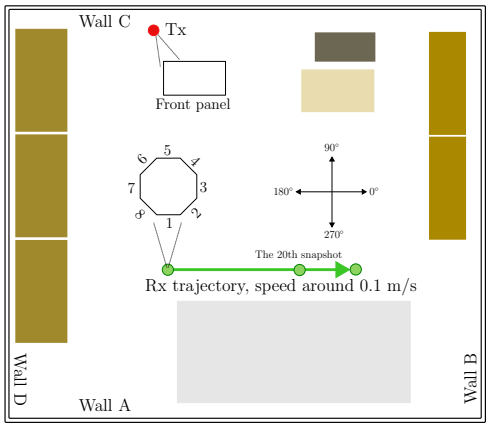

(b)

Fig. 12. The dynamic propagation channel measurement in an indoor laboratory scenario where the Rx speed was around 0.1 m/s. (a) A panoramic picture taken during the measurement. (b) A layout of the Tx location, the Rx movement trajectory, and array orientations during the measurement.

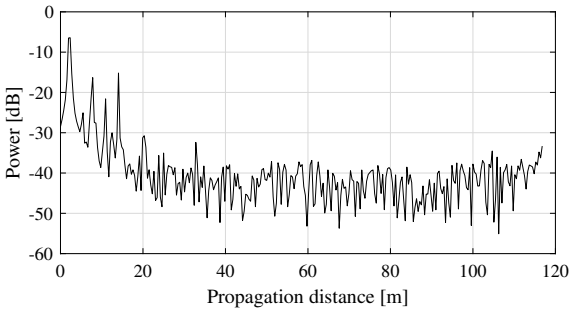

(a)

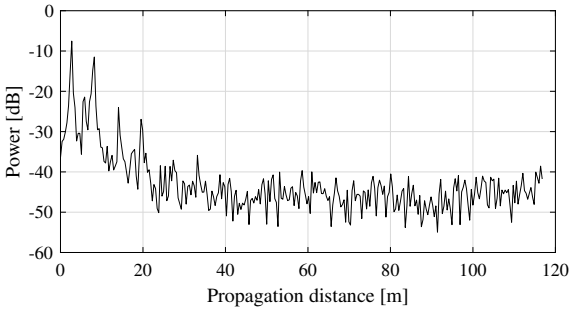

(b)

Fig. 13. The channel impulse response with processing gains. (a) The first snapshot. (b) The twentieth snapshot.

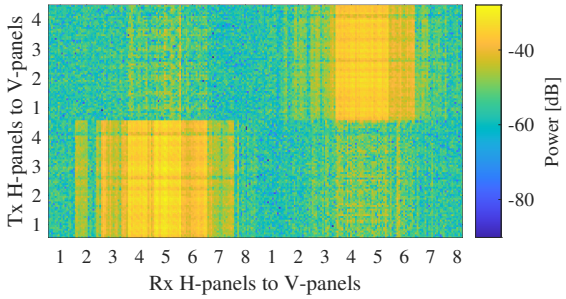

(a)

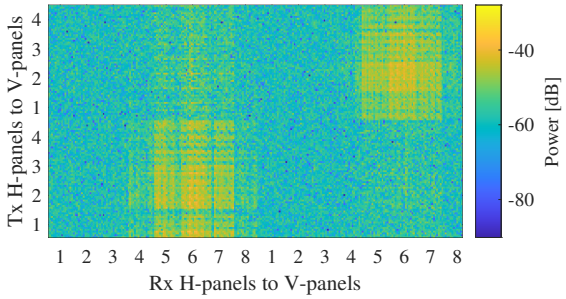

(b)

Fig. 14. The received power at the LoS delay bin of channel impulse responses measured at all antenna combinations. (a) The first snapshot. (b) The twentieth snapshot.

where all the processing gains as indicated in Fig. 11 have been harvested. It can be observed that the received power decreased from the first to the twentieth snapshot due to Tx-Rx distance increasing, and several different peaks (paths) existed in both channels. Fig. 14 illustrates the powers received at the line-of-sight (LoS) delay bins of channel impulse responses measured at all antenna combinations, for the first snapshot and the twentieth snapshot, respectively. It can be observed that the LoS path impinged mainly into Rx panels 4-6 at the first snapshot and mainly panels 5-7 at the twentieth snapshot, which is consistent with the geometry. Moreover, higher received power was observed only when the transmit antenna and the receive antenna have the same primary polarization.

Fig. 15, as an example, illustrates the high-resolution estimation results of MPCs for the first snapshot. The AoDs and AoAs of the LoS path (with the strongest gain) is consistent with the geometry. There are also many more non-LoS (NLoS) paths observed. We can, e.g., observe two MPCs with propagation distances of around 4 m, elevations at both sides of around 50°, and azimuths at both sides almost the same to the LoS path. It can be inferred with good confidence that they were caused by the ceiling.

Fig. 16 concatenates all the MPCs of all snapshots in different parameter domains, showing a clear evolution of these MPCs. It is obvious that the channel parameters became stable for the last six snapshots when the Rx stopped moving. It can also be observed that the propagation distance of the LoS path-trajectory increased along the trajectory. Its elevations at both sides were kept at around 90° due to the same heights of arrays, and azimuths at both sides were getting larger as

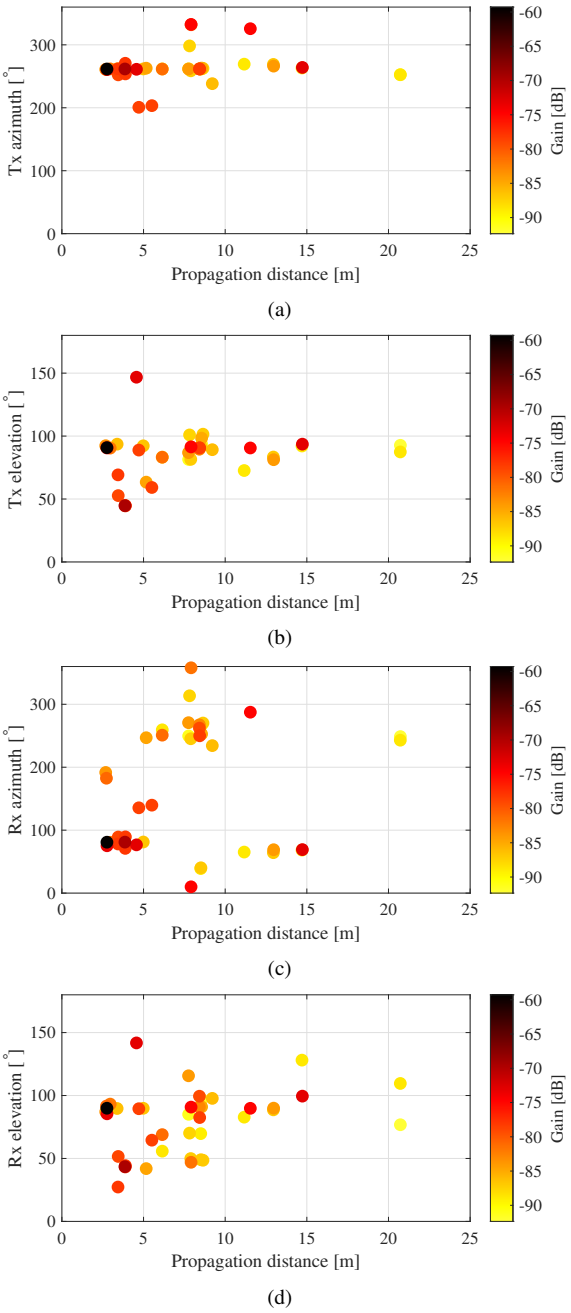

Fig. 15. High-resolution propagation channel parameter estimation results of MPCs observed at the first snapshot. (a) Propagation-distance Tx-azimuth power spectrum. (b) Propagation-distance Tx-elevation power spectrum. (c) Propagation-distance Rx-azimuth power spectrum. (d) Propagation-distance Rx-elevation power spectrum.

expected. There was another obvious trajectory with larger delays compared to the LoS trajectory. Its elevations were also kept around 90°, and its azimuths at the Tx sides were also increasing with a slower slope compared to that of LoS path. However, its azimuths at the Rx sides were decreasing. It can be well inferred that this path is due to the reflection of Wall A as indicated in Fig. 12. Similarly, other trajectories can be tracked and mapped to their corresponding physical scatterers in the scenario. A sophisticated tracking algorithm using belief propagation can be found in [71]. Naturally, many further details from the measured results can be analyzed. However, we refrain from doing this, since the central focus of the paper is on the design, implementation and measurement-based verification of the proposed sounder. Interested readers can also refer to [72, 73] for more information, where the validity of the sounder is further verified in a building yard by investigating the physical interacting points of the measured channels and conducting a successful radio-based simultaneous mapping and localization, respectively.

V. Conclusions

We presented a novel mmWave propagation channel sounder based on the switched array principle. It can measure 128×256 MIMO channels within a short measurement time of around 600 ms. Unlike previously presented mmWave sounders, the proposed design offers the highest degree of reconfigurability, and compliments the high delay resolution with high-resolution spatial characteristics provided by the uniquely designed transmit and receive arrays. We can accurately characterize amplitudes, delays, angles, Doppler and polarization parameters of propagation paths of dynamic mmWave channels. Moreover, via careful RF design, negligible phase drift is seen between the reference local oscillators (LOs) at both link ends, even in the absence of a cabled connection for timing synchronization. This enables averaging multiple complex waveforms to enhance the measurement signal-to-noise ratio (SNR) - something which is particularly valuable for measurements that require a large dynamic range. Using a high-resolution parameter estimation algorithm, we extracted the propagation parameters of multipath components measured in the laboratory scenario. The consistency of the channel behavior in different parameter domains to the propagation scenario verifies the designed sounder.

References

[1] Z. Ying, K. Zhao, E. Bengtsson, H. Tataria, and F. Tufvesson, "Design of switched antenna arrays for a 28 GHz propagation channel sounder," in *IEEE International Symposium on Antennas and Propagation and North American Radio Science Meeting*, 2020, pp. 55–56.

[2] E. L. Bengtsson, "Massive MIMO from a terminal perspective," Ph.D. thesis, Lund University, Sep. 2019.

[3] X. Cai, X. Cheng, and F. Tufvesson, "Toward 6G with terahertz communications: Understanding the propagation channels," *IEEE Communications Magazine*, vol. 62, no. 2, pp. 32–38, 2024.

[4] T. S. Rappaport, G. R. MacCartney, M. K. Samimi, and S. Sun, "Wideband millimeter-wave propagation measurements and channel models for future wireless communication system design," *IEEE Transactions on Communications*, vol. 63, no. 9, pp. 3029–3056, 2015.

[5] H. Tataria *et al.*, "6G wireless systems: Vision, requirements, challenges, insights, and opportunities," *Proceedings of the IEEE*, vol. 109, no. 7, pp. 1166–1199, 2021.

[6] M. Shafi *et al.*, "Microwave vs. millimeter-wave propagation channels: Key differences and impact on 5G cellular systems," *IEEE Communications Magazine*, vol. 56, no. 12, pp. 14–20, 2018.

[7] FCC, "Technical report on auction 102 for spectrum frontiers - 24 GHz," May 2019.

[8] 3GPP TR 21.95 v1.1.0, "Technical specification group services and system aspects for release 15," March 2019.

[9] ITU-R M.2083-0, "IMT-2020 vision - framework and overall objectives of the future development of IMT for 2020 and beyond," ITU-R, Sep 2015.

[10] R. M. Dreifuerst and R. W. Heath, "Massive MIMO in 5G: How beamforming, codebooks, and feedback enable larger arrays," 2023. [Online]. Available: https://arxiv.org/abs/2301.13390

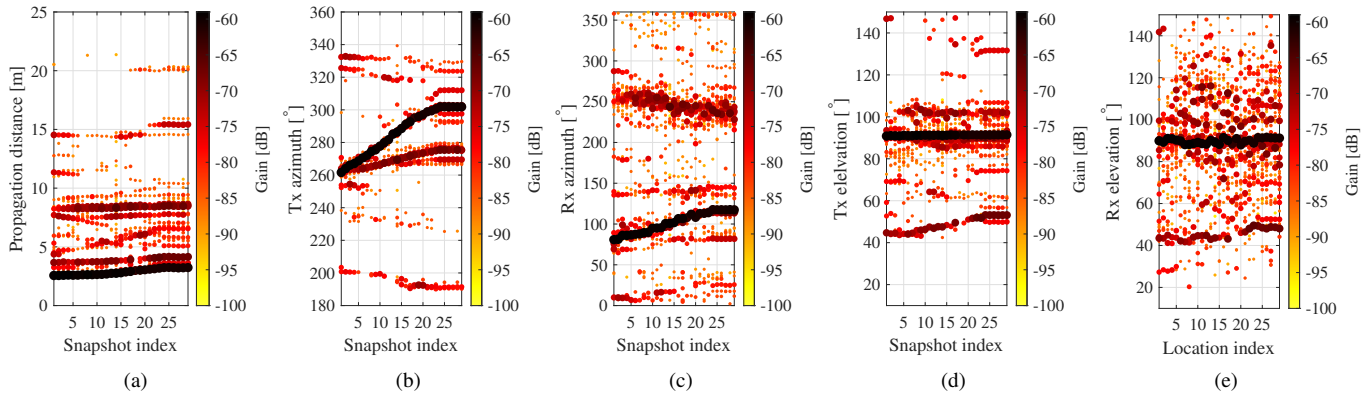

Fig. 16. Concatenated MPCs estimated for all snapshots along the trajectory, where the Rx was static for the last six snapshots. (a) Propagation distance domain. (b) Tx azimuth domain. (c) Rx azimuth domain. (d) Tx elevation domain. (e) Rx elevation domain.

[11] X. Cai *et al.*, "Dynamic mmWave channel emulation in a cost-effective MPAC with dominant-cluster concept," *IEEE Transactions on Antennas and Propagation*, vol. 70, no. 6, pp. 4691–4704, 2022.

[12] IEEE Standard Association, Channel Models of Wireless Systems (COM/MobiNet-SC/CMWG) Working Group, "Standard for channel models of wireless systems," Project number P1944. [Online]. Available: https://development.standards.ieee.org/myproject-web/public/view.html#pardetail/10557

[13] IEEE Standard Association, Millimeter-Wave Channel Sounder Verification (VT/ITS/MMW-CSV) Working Group, "Millimeter-wave channel sounder verification," Project number P2982. [Online]. Available: https://development.standards.ieee.org/myproject-web/public/view.html#pardetail/8961

[14] P. Smulders and A. Wagemans, "Wide-band measurements of mm-wave indoor radio channels," in *IEEE International Symposium on Personal, Indoor and Mobile Radio Communications*, 1992, pp. 329–333.

[15] C. Gustafson, F. Tufvesson, S. Wyne, K. Haneda, and A. F. Molisch, "Directional analysis of measured 60 GHz indoor radio channels using SAGE," in *IEEE 73rd Vehicular Technology Conference (VTC Spring)*, 2011, pp. 1–5.

[16] C. Gustafson and F. Tufvesson, "Characterization of 60 GHz shadowing by human bodies and simple phantoms," in *European Conference on Antennas and Propagation (EUCAP)*, 2012, pp. 473–477.

[17] W. Fu, J. Hu, and S. Zhang, "Frequency-domain measurement of 60 GHz indoor channels: a measurement setup, literature data, and analysis," *IEEE Instrumentation & Measurement Magazine*, vol. 16, no. 2, pp. 34–40, 2013.

[18] J. Blumenstein *et al.*, "In-vehicle channel measurement, characterization, and spatial consistency comparison of 30-11 GHz and 55-65 GHz frequency bands," *IEEE Transactions on Vehicular Technology*, vol. 66, no. 5, pp. 3526–3537, 2017.

[19] J. Medbo, H. Asplund, and J.-E. Berg, "60 GHz channel directional characterization using extreme size virtual antenna array," in *IEEE 26th Annual International Symposium on Personal, Indoor, and Mobile Radio Communications (PIMRC)*, 2015, pp. 176–180.

[20] A. W. Mbugua, W. Fan, K. Olesen, X. Cai, and G. F. Pedersen, "Phase-compensated optical fiber-based ultrawideband channel sounder," *IEEE Transactions on Microwave Theory and Techniques*, vol. 68, no. 2, pp. 636–647, 2020.

[21] X. Cai *et al.*, "Dynamic channel modeling for indoor millimeter-wave propagation channels based on measurements," *IEEE Transactions on Communications*, vol. 68, no. 9, pp. 5878–5891, 2020.

[22] T. S. Rappaport *et al.*, "Broadband millimeter-wave propagation measurements and models using adaptive-beam antennas for outdoor urban cellular communications," *IEEE Transactions on Antennas and Propagation*, vol. 61, no. 4, pp. 1850–1859, 2013.

[23] S. Hur *et al.*, "Synchronous channel sounder using horn antenna and indoor measurements on 28 GHz," in *IEEE International Black Sea Conference on Communications and Networking (BlackSeaCom)*, 2014, pp. 83–87.

[24] J. Ko *et al.*, "Millimeter-wave channel measurements and analysis for statistical spatial channel model in in-building and urban environments at 28 GHz," *IEEE Transactions on Wireless Communications*, vol. 16, no. 9, pp. 5853–5868, 2017.

[25] G. R. MacCartney and T. S. Rappaport, "A flexible millimeter-wave channel sounder with absolute timing," *IEEE Journal on Selected Areas in Communications*, vol. 35, no. 6, pp. 1402–1418, 2017.

[26] J. Du *et al.*, "Suburban residential building penetration loss at 28 GHz for fixed wireless access," *IEEE Wireless Communications Letters*, vol. 7, no. 6, pp. 890–893, 2018.

[27] M.-D. Kim, J. Liang, Y. K. Yoon, and J. H. Kim, "28 GHz path loss measurements in urban environments using wideband channel sounder," in *IEEE International Symposium on Antennas and Propagation & USNC/URSI National Radio Science Meeting*, 2015, pp. 1798–1799.

[28] R. Müller, R. Herrmann, D. A. Dupleich, C. Schneider, and R. S. Thomä, "Ultrawideband multichannel sounding for mm-wave," in *European Conference on Antennas and Propagation (EuCAP 2014)*, 2014, pp. 817–821.

[29] D. Dupleich *et al.*, "Multi-band propagation and radio channel characterization in street canyon scenarios for 5G and beyond," *IEEE Access*, vol. 7, pp. 160 385–160 396, 2019.

[30] P. B. Papazian, C. Gentile, K. A. Remley, J. Senic, and N. Golmie, "A radio channel sounder for mobile millimeter-wave communications: System implementation and measurement assessment," *IEEE Transactions on Microwave Theory and Techniques*, vol. 64, no. 9, pp. 2924–2932, 2016.

[31] R. Sun *et al.*, "Design and calibration of a double-directional 60 GHz channel sounder for multipath component tracking," in *11th European Conference on Antennas and Propagation (EUCAP)*, 2017, pp. 3336–3340.

[32] S. Salous, "Multi-band multi-antenna chirp channel sounder for frequencies above 6 GHz," in *10th European Conference on Antennas and Propagation (EuCAP)*, 2016, pp. 1–4.

[33] S. Salous, S. M. Feeney, X. Raimundo, and A. A. Cheema, "Wideband MIMO channel sounder for radio measurements in the 60 GHz band," *IEEE Transactions on Wireless Communications*, vol. 15, no. 4, pp. 2825–2832, 2016.

[34] Z. Wen *et al.*, "mmWave channel sounder based on COTS instruments for 5G and indoor channel measurement," in *IEEE Wireless Communications and Networking Conference*, 2016, pp. 1–7.

[35] D. He *et al.*, "Influence analysis of typical objects in rural railway environments at 28 GHz," *IEEE Transactions on Vehicular Technology*, vol. 68, no. 3, pp. 2066–2076, 2019.

[36] G. R. MacCartney, T. S. Rappaport, and S. Rangan, "Rapid fading due to human blockage in pedestrian crowds at 5G millimeter-wave frequencies," in *IEEE Global Communications Conference*, 2017, pp. 1–7.

[37] C. U. Bas *et al.*, "Real-time millimeter-wave MIMO channel sounder for dynamic directional measurements," *IEEE Transactions on Vehicular Technology*, vol. 68, no. 9, pp. 8775–8789, 2019.

[38] N. Deparis *et al.*, "Transposition of a baseband UWB signal at 60 GHz for high data rate indoor WLAN," *IEEE Microwave and Wireless Components Letters*, vol. 15, no. 10, pp. 609–611, 2005.

[39] U. Demir and S. C. Ergen, "ARIMA-based time variation model for beneath the chassis UWB channel," *EURASIP Journal on Wireless Communications and Networking*, vol. 2016, no. 1, p. 178, Aug 2016.

[40] D. Cassioli, "60 GHz UWB channel measurement and model," in *IEEE International Conference on Ultra-Wideband*, 2012, pp. 145–149.

[41] T. Zwick, T. Beukema, and H. Nam, "Wideband channel sounder with measurements and model for the 60 GHz indoor radio channel," *IEEE*

Transactions on Vehicular Technology, vol. 54, no. 4, pp. 1266–1277, 2005.
[42] J. E. Håkegård, H. Rustad, I. Tardy, T. A. Myrvoll, and V. Ringset, "mm-wave channel sounding using a fully programmable SoC," in *IEEE 27th Annual International Symposium on Personal, Indoor, and Mobile Radio Communications (PIMRC)*, 2016, pp. 1–6.
[43] A. Prokes *et al.*, "Time-domain nonstationary intra-car channel measurement in 60 GHz band," in *International Conference on Advanced Technologies for Communications (ATC)*, 2016, pp. 1–6.
[44] J.-M. Conrat, P. Pajusco, and J.-Y. Thiriet, "A multibands wideband propagation channel sounder from 2 to 60 GHz," in *IEEE Instrumentation and Measurement Technology Conference Proceedings*, 2006, pp. 590–595.
[45] M. Friese, "Multitone signals with low crest factor," *IEEE Transactions on Communications*, vol. 45, no. 10, pp. 1338–1344, 1997.
[46] Peregrine Semiconductors: Portfolio of RF Switches, accessed on Feb. 7, 2023. [Online]. Available: http://www.psemi.com/products/rf-switches
[47] R. Sun *et al.*, "Millimeter-wave radio channels vs. synthetic beamwidth," *IEEE Communications Magazine*, vol. 56, no. 12, pp. 53–59, 2018.
[48] C. Gentile *et al.*, "Millimeter-wave channel measurement and modeling: A NIST perspective," *IEEE Communications Magazine*, vol. 56, no. 12, pp. 30–37, 2018.
[49] J. Ala-Laurinaho *et al.*, "2-D beam-steerable integrated lens antenna system for 5G E-band access and backhaul," *IEEE Transactions on Microwave Theory and Techniques*, vol. 64, no. 7, pp. 2244–2255, 2016.
[50] J. Zhang *et al.*, "3D MIMO for 5G NR: Several observations from 32 to massive 256 antennas based on channel measurement," *IEEE Communications Magazine*, vol. 56, no. 3, pp. 62–70, 2018.
[51] G.-S. Shin *et al.*, "Low insertion loss, compact 4-bit phase shifter in 65 nm CMOS for 5G applications," *IEEE Microwave and Wireless Components Letters*, vol. 26, no. 1, pp. 37–39, 2016.
[52] AT&T, "AT&T debuts 5G channel sounder "porcupinea" with NI," Aug. 2019. [Online]. Available: http://www.fiercewireless.com/wireless/at-t-debuts-5g-channel-sounder-porcupine-ni
[53] X. Yin, B. Fleury, P. Jourdan, and A. Stucki, "Doppler frequency estimation for channel sounding using switched multiple-element transmit and receive antennas," in *IEEE Global Telecommunications Conference*, vol. 4, 2003, pp. 2177–2181 vol.4.
[54] A. Al-Ameri, J. Park, J. Sanchez, X. Cai, and F. Tufvesson, "A hybrid antenna switching scheme for dynamic channel sounding," in *IEEE 97th Vehicular Technology Conference (VTC2023-Spring)*, 2023, pp. 1–6.
[55] T. Pedersen *et al.*, "Joint estimation of doppler frequency and directions in channel sounding using switched tx and rx arrays," in *IEEE Global Telecommunications Conference*, vol. 4, 2004, pp. 2354–2360 Vol.4.
[56] T. Pedersen, C. Pedersen, X. Yin, and B. H. Fleury, "Optimization of spatiotemporal apertures in channel sounding," *IEEE Transactions on Signal Processing*, vol. 56, no. 10, pp. 4810–4824, 2008.
[57] R. Wang, O. Renaudin, C. U. Bas, S. Sangodyin, and A. F. Molisch, "Antenna switching sequence design for channel sounding in a fast time-varying channel," in *IEEE International Conference on Communications (ICC)*, 2018, pp. 1–6.
[58] M. Ivashina *et al.*, "A 1-D steerable beam slotted waveguide antenna employing non-conventional aperiodic array architecture for mm-wave line-of-sight MIMO," in *IEEE International Conference on Microwaves, Antennas, Communications and Electronic Systems (COMCAS)*, 2019, pp. 1–4.
[59] Stanford Research Systems: Frequency Standards FS725 — Benchtop rubidium frequency standard. [Online]. Available: https://www.thinksrs.com/downloads/pdfs/catalog/FS725c.pdf
[60] M. Feder and E. Weinstein, "Parameter estimation of superimposed signals using the em algorithm," *IEEE Transactions on Acoustics, Speech, and Signal Processing*, vol. 36, no. 4, pp. 477–489, 1988.
[61] B. Fleury, M. Tschudin, R. Heddergott, D. Dahlhaus, and K. Ingeman Pedersen, "Channel parameter estimation in mobile radio environments using the SAGE algorithm," *IEEE Journal on Selected Areas in Communications*, vol. 17, no. 3, pp. 434–450, 1999.
[62] R. Vaughan and N. Scott, "Super-resolution of pulsed multipath channels for delay spread characterization," *IEEE Transactions on Communications*, vol. 47, no. 3, pp. 343–347, 1999.
[63] A. Richter, "Estimation of radio channel parameters: Models and algorithms," Ph.D. dissertation, Technische Universität Ilmenau, Germany, 2005. [Online]. Available: https://www.db-thueringen.de/servlets/MCRFileNodeServlet/dbt_derivate_00007407/ilm1-2005000111.pdf
[64] H. Tataria *et al.*, "Channel correlation diversity in MU-MIMO systems – analysis and measurements," in *IEEE 30th Annual International Symposium on Personal, Indoor and Mobile Radio Communications (PIMRC)*, 2019, pp. 1–7.
[65] S. Sangodoyin *et al.*, "Cluster characterization of 3-D MIMO propagation channel in an urban macrocellular environment," *IEEE Transactions on Wireless Communications*, vol. 17, no. 8, pp. 5076–5091, 2018.
[66] X. Cai and W. Fan, "A complexity-efficient high resolution propagation parameter estimation algorithm for ultra-wideband large-scale uniform circular array," *IEEE Transactions on Communications*, vol. 67, no. 8, pp. 5862–5874, 2019.
[67] X. Cai, W. Fan, X. Yin, and G. F. Pedersen, "Trajectory-aided maximum-likelihood algorithm for channel parameter estimation in ultrawideband large-scale arrays," *IEEE Transactions on Antennas and Propagation*, vol. 68, no. 10, pp. 7131–7143, 2020.
[68] X. Cai, M. Zhu, A. Fedorov, and F. Tufvesson, "Enhanced effective aperture distribution function for characterizing large-scale antenna arrays," 2022. [Online]. Available: https://arxiv.org/abs/2209.11483
[69] M. Landmann, A. Richter, and R. Thoma, "DoA resolution limits in MIMO channel sounding," in *IEEE Antennas and Propagation Society Symposium*, vol. 2, 2004, pp. 1708–1711.
[70] X. Cai *et al.*, "Enabling complexity-efficient high-resolution parameter estimation for wideband switched array channel sounding," *Under preparation*, 2023.
[71] X. Li, E. Leitinger, A. Venus, and F. Tufvesson, "Sequential detection and estimation of multipath channel parameters using belief propagation," *IEEE Transactions on Wireless Communications*, vol. 21, no. 10, pp. 8385–8402, 2022.
[72] H. Khosravi, X. Cai, and F. Tufvesson, "Experimental analysis of physical interacting objects of a building at mmWave frequencies," in *18th European Conference on Antennas and Propagation (EuCAP)*, 2024, pp. 1–5.
[73] X. Li, X. Cai, E. Leitinger, and F. Tufvesson, "A belief propagation algorithm for multipath-based SLAM with multiple map features: A mmWave MIMO application," in *IEEE International Conference on Communications, accepted, arXiv:2403.10095*, 2024, pp. 1–6.

Xuesong Cai (Senior Member, IEEE) received the B.S. degree and the Ph.D. degree (with distinction) from Tongji University, Shanghai, China, in 2013 and 2018, respectively. In 2015, he conducted a three-month internship with Huawei Technologies, Shanghai, China. He was also a Visiting Scholar with Universidad Politécnica de Madrid, Madrid, Spain in 2016. From 2018-2022, he conducted several postdoctoral stays at Aalborg University and Nokia Bell Labs, Denmark, and Lund University, Sweden. He is currently an Assistant Professor in Communications Engineering and a Marie Skłodowska-Curie Fellow at Lund University, closely cooperating with Ericsson and Sony. His research interests include radio propagation, high-resolution parameter estimation, over-the-air testing, resource optimization, and radio-based localization for 5G/B5G wireless systems. His work has led to over 66 peer-reviewed publications, 2 book chapters, and 4 granted patents.

Dr. Cai was a recipient of the China National Scholarship (the highest honor for Ph.D. Candidates) in 2016, the Outstanding Doctorate Graduate awarded by the Shanghai Municipal Education Commission in 2018, the Marie Skłodowska-Curie Actions (MSCA) "Seal of Excellence" in 2019, the EU MSCA Fellowship (ranking top 1.2%, overall success rate 14%) and the Starting Grant (success rate 12%) funded by the Swedish Research Council in 2022. He was also selected by the "ZTE Blue Sword-Future Leaders Plan" in 2018 and the "Huawei Genius Youth Program" in 2021. He is an AP-S 2024 Young Professional Ambassador and serves as an Editor of IEEE Transactions on Vehicular Technology, IEEE Antennas and Wireless Propagation Letters, and IET Communications.

Erik L. Bengtsson received M. Sc. and Ph.D. in Electrical Engineering from Lund University 1997 and 2019 respectively. He joined Ericsson in Lund 1997 and worked with RF ASIC design until 2005 when he joined Nokia A/S in Copenhagen, there he worked with concept development of reconfigurable antennas. In 2011 Erik joined Sony in Lund and between 2015-2019 he was an industry Ph.D. student at the Department of Electrical and Information Technology at Lund University. Erik is currently managing a research team at Sony and his current research interests include RIS, massive MIMO, and radio channel characterization. He has worked with 3GPP standardization since 2014 with a focus on MIMO.

Ove Edfors (Senior Member, IEEE) is currently a Professor in radio systems with the Department of Electrical and Information Technology, Lund University, Lund, Sweden. His current research interests include statistical signal processing and low-complexity algorithms with applications in wireless communications. In the context of massive MIMO, his main research interests include how realistic propagation characteristics influence system performance and baseband processing complexity.

Fredrik Tufvesson (Fellow, IEEE) received the Ph.D. degree from Lund University, Lund, Sweden, in 2000.

After two years at a startup company, he joined the Department of Electrical and Information Technology, Lund University, where he is currently a Professor of radio systems. He has authored around 100 journal articles and 150 conference papers. His main research interest is the interplay between the radio channel and the rest of the communication system with various applications in 5G/B5G systems, such as massive multiple-input multiple-output (MIMO), mmWave communication, vehicular communication, and radio-based positioning.

Dr. Tufvesson's research has been awarded the Neal Shepherd Memorial Award for the Best Propagation Paper in the IEEE TRANSACTIONS ON VEHICULAR TECHNOLOGY and the IEEE Communications Society Best Tutorial Paper Award.